ELSEVIER Journal of Electron Spectroscopy and Related Phenomena 117–118 (2001) 347–369

JOURNAL OF ELECTRON SPECTROSCOPY and Related Phenomena

www.elsevier.nl/locate/elspec

Comparative study of the electronic structure of XRu_2Si_2: probing the Anderson lattice

J.D. Denlinger[a,*], G.-H. Gweon[b], J.W. Allen[b], C.G. Olson[c], M.B. Maple[d], J.L. Sarrao[e], P.E. Armstrong[e], Z. Fisk[f], H. Yamagami[g]

[a] *Advanced Light Source, Lawrence Berkeley National Lab, Berkeley, CA 94720, USA*
[b] *Randall Laboratory, University of Michigan, Ann Arbor, MI 48109-1120, USA*
[c] *Ames Laboratory, Iowa State University, Ames, IA 50011, USA*
[d] *Department of Physics, and Institute for Pure and Applied Physical Sciences, University of California at San Diego, La Jolla, CA 92093, USA*
[e] *Los Alamos National Laboratory, Los Alamos, NM 87545, USA*
[f] *National High Magnetic Field Lab and Department of Physics, Florida State University, Tallahassee, FL 32306, USA*
[g] *Kyoto-Sangyo University, Kyoto, Japan*

Received 9 August 2000; accepted 26 December 2000

Abstract

The **k**-resolved single particle excitations, as determined by angle-resolved photoemission spectroscopy (ARPES), are compared and contrasted for, $LaRu_2Si_2$, $CeRu_2Si_2$, $ThRu_2Si_2$, and URu_2Si_2, isostructural layered compounds with differing nominal *f*-occupations of f^0, f^1, f^0, and f^2, respectively. ARPES measurements include 4*d* and 5*d*-edge resonant photoemission to distinguish *f*-character and Fermi-energy intensity mapping of Fermi surface contours. Comparison to RLAPW band structure calculations shows very good agreement of the *d*-band structure away from E_F. Discrepancies in the near E_F region highlight **k**-dependent effects of *f*-correlation and *f*–*d* hybridization. Approximately equal dimensions of Fermi contours for X=(La, Ce) suggest the exclusion of 4*f* electrons from the $CeRu_2Si_2$ Fermi surface at temperatures far above the Kondo temperature. High-resolution spectra for X=(Ce, U) allow comparison of *f*–*d* mixing to predictions of the Anderson lattice model. Published by Elsevier Science B.V.

Keywords: Angle resolved photoemission; *f*-electron; Heavy fermion; Anderson lattice

1. Introduction

Mixed valent and heavy-fermion *f*-electron materials manifest a challenging interplay of atomic and electron gas physics, generally understood to involve hybridization between localized *f*-orbitals and other band-like *s*, *p* or *d*-states of the solid. For a single material, some properties, e.g. Kondo effects, can be described by the impurity Anderson model, and yet the *f*-electrons contribute to the heavy-mass Fermi surface (FS) [1–4]. One theoretical approach to the FS utilizes the band structure calculated in the local density approximation (LDA), including the *f*-electrons, but renormalizing their scattering phase shifts at the FS to be Kondo-like. This procedure gives heavy masses, and often makes only a minor per-

*Corresponding author. Tel.: +1-510-486-5648; fax: +1-510-486-7588.
E-mail address: jddenlinger@lbl.gov (J.D. Denlinger).

0368-2048/01/$ – see front matter Published by Elsevier Science B.V.
PII: S0368-2048(01)00257-2

turbation of the original LDA FS [5]. Alternatively, results based on theoretical treatments of the Anderson lattice Hamiltonian [6–8] suggest a model with a renormalized *f*-level just above E_F, and renormalized hybridization to the *s–p–d* band structure. The two renormalizations reflect the Kondo effect. Two-band mixing very near E_F then shifts the $\mathbf{k}_F$ value somewhat and enhances the effective mass at $\mathbf{k}_F$, but the overall FS topology appears to be largely determined by the underlying *s–p–d* band structure in the absence of hybridization to the *f*-states. Although the two approaches must yield the same FS volume to count electrons correctly, it is not a priori obvious that they yield the same FS topology.

Angle integrated electron spectroscopy has been very successful in revealing single-ion properties [9,10], while quantitative FS information has been obtained only by magneto-oscillatory (MO) techniques such as the de Haas–van Alphen (dHvA) effect [11,12]. MO techniques do not provide a global view of the energy and **k**-dependence of the electronic structure, and so are limited for distinguishing among different theoretical scenarios of heavy mass FS formation. Angle-resolved photoemission spectroscopy (ARPES) in principle provides this global view. Momentum-dependent effects have been reported in ARPES studies of *f*-electron systems, e.g. high-resolution He I valence band measurements [13,14], amplitude variations of the near-E_F 4*f*-weight periodic with the Brillouin zone [15,16] and claims of ''band-like'' dispersion of *f*-states [17,18]. However, because of technical barriers, ARPES has never provided enough FS detail in these systems for its potential to be realized.

Recent advances in photoemission instrumentation and techniques are beginning to overcome these barriers. One direction has been to push the photoemission technique close to its ultimate energy resolution at very low temperatures in order to access the small energy scales of the Kondo effect [19]. Another direction has been to improve the energy resolution at ~ 1 keV photon energies in order probe more bulk-sensitive valence structure [20]. The key advance exploited in the work described here is the recent ability to perform moderately high-resolution ARPES measurements at photon energies greater than 100 eV. This extended photon energy range is essential for adequate k-space coverage of three dimensional materials and also gives access to the strong $4d \rightarrow 4f$ and $5d \rightarrow 5f$ resonances that are commonly used to distinguish *f* character in angle-integrated photoemission [9]. This powerful combination of ARPES and resonant photoemission (ResPES) is additionally greatly enhanced by the use of the Fermi-energy intensity mapping technique that provides a visualization of the global **k**-dependence of *f*-weight in multiple Brilloun zones and a detailed correspondence to the *d*-band structure. URu_2Si_2 is the first *f*-electron system to receive detailed experimental treatment with the above combination of photoemission techniques [21].

In testing theoretical models of heavy mass FS formation it is also very important to compare similar systems with varying *f* occupation because LDA band calculations done for varying numbers of *f*-electrons in the valence band show systematic differences in the Fermi surface topologies. The XRu_2Si_2 system with X=(La, Ce, Th, U) is a favorable isostructural series for the comparison of band structure and FS topology with only the 4*f* or 5*f* occupation being varied. $LaRu_2Si_2$ is a $4f^0$ rare-earth system with 3^+ valence. $CeRu_2Si_2$ is a $4f^1$ heavy fermion system ($\gamma = 350$ mJ/mol-K^2) with 3^+ valence and is a prime literature example of very good agreement between renormalized LDA band calculations and dHvA Fermi surface and effective mass measurements [22,23]. $ThRu_2Si_2$ is a $5f^0$ actinide system with 4^+ valence. URu_2Si_2 is a nominally $5f^2$ system with a moderately large linear specific heat coefficient of $\gamma = 180$ mJ/mol-K^2 extrapolated from the paramagnetic phase [24,25]. In addition, URu_2Si_2 is anti-ferromagnetic below 17.5 K and superconducting below 1.2 K. The theoretical interest in these low temperature phase transitions including the coexistence of magnetism and superconductivity has resulted in URu_2Si_2 being one of the most heavily studied 5*f* systems, continuing up to the present [26]. In this paper, the experimental FS topologies and valence band structures of the four XRu_2Si_2 systems are systematically compared with each other, with LDA band structure calculations, and with expectations from the Anderson lattice model. Only paramagnetic URu_2Si_2 is studied here.

The paper is organized as follows. The framework for discussion of the ARPES data is provided by Section 1.1 which compares the calculated LDA

band structures of the four compounds and discusses theoretical approaches that go beyond LDA, including qualitative predictions of the Anderson lattice model. Section 1.2 presents the important experimental details, including the locations in **k**-space being probed by ARPES. In Section 2, the experimental and theoretical band structures and Fermi surface topologies are compared for the 4*f* rare earth systems. Off-resonance comparison of FS maps for X=(La, Ce) is shown to give evidence for the interesting conjecture that the *f* electrons are excluded from the FS in $CeRu_2Si_2$ at temperatures far above the Kondo temperature. On-resonance ARPES and FS maps show the **k**-space correlation of 4*f*-weight to the underlying *d*-band dispersions and FS. In Section 3, comparison of the two 5*f* actinide systems is used to discuss the origins of major discrepancies between ARPES and LDA for URu_2Si_2. Section 4 focuses on the *f*-weight distribution at isolated regions of **k**-space for X=(Ce, U) with a qualitative comparison to Anderson lattice model predictions of *f*–*d* mixing. Preliminary temperature-dependent data for URu_2Si_2 showing Kondo-like behavior and a brief discussion of surface effects are also presented.

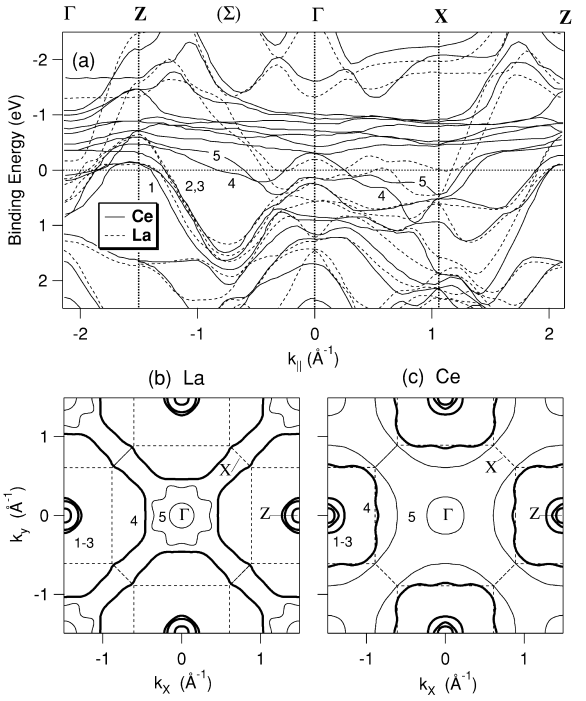

Fig. 1. Comparison of (a) theoretical LDA band structures and (b, c) 2-D Fermi-surface contours for $LaRu_2Si_2$ and $CeRu_2Si_2$. Bold (thin) contours in (b) and (c) correspond to hole (electron) FS topologies and dashed lines are Brillouin zone boundaries. Bands that cross E_F and FS contours are numbered for clarity.

1.1. Theory

Figs. 1 and 2 show a comparison of the LDA band structures and FS's for the four XRu_2Si_2 compounds. We will use these comparisons to highlight the theoretical issues to be addressed experimentally. The displayed high-symmetry directions of Γ–Z, Z–(Σ)–Γ, and Γ–X correspond to the ⟨001⟩, ⟨100⟩ and ⟨110⟩ directions of the body-centered tetragonal (bct) Brillouin zone (BZ). The X–Z direction is orthogonal to Γ–X and completes an in-plane triangle. The FS cross-sections are centered at Γ. The energy band calculations for $ThRu_2Si_2$ and URu_2Si_2 were performed using a relativistic linear-augmented plane-wave (RLAPW) method [27], while a fully-relativistic symmetrized-APW method [28] was employed for $LaRu_2Si_2$ and $CeRu_2Si_2$. Both methods include LDA exchange-correlation potentials in the relativistic Dirac equation, which is directly solved without a perturbation treatment of the spin–orbit interaction. The angular dependences of the Fermi surface frequency branches of the de Haas–van Alphen effect have previously been explained reasonably well by these calculations for $LaRu_2Si_2$ [29] and $CeRu_2Si_2$ [30]. The band structures and Fermi surfaces in this paper are in good agreement with other relativistic LDA calculations for $CeRu_2Si_2$ [31] and URu_2Si_2 [32].

Common to all four systems is the parabolic dispersion of a cluster of three bands centered along Z–(Σ)–Γ with a band minimum of ≈1.5 eV binding energy. These bands of mostly Ru 4*d* character (labeled 1–3 in Fig. 1) approach E_F at the Z-point and form small concentric FS hole pockets. In both cases of $LaRu_2Si_2$ and $CeRu_2Si_2$, all three bands cross E_F near the Z-point, while for $ThRu_2Si_2$, one band does not reach E_F and for URu_2Si_2 none of the three bands cross E_F. Near the Γ-point, these same *d*-bands (1–3) hybridize with another pair of bands (4,5) dispersing downward from above E_F, creating a more complicated electronic structure in this region. Bands 4 and 5 and their continuation along Γ–X give

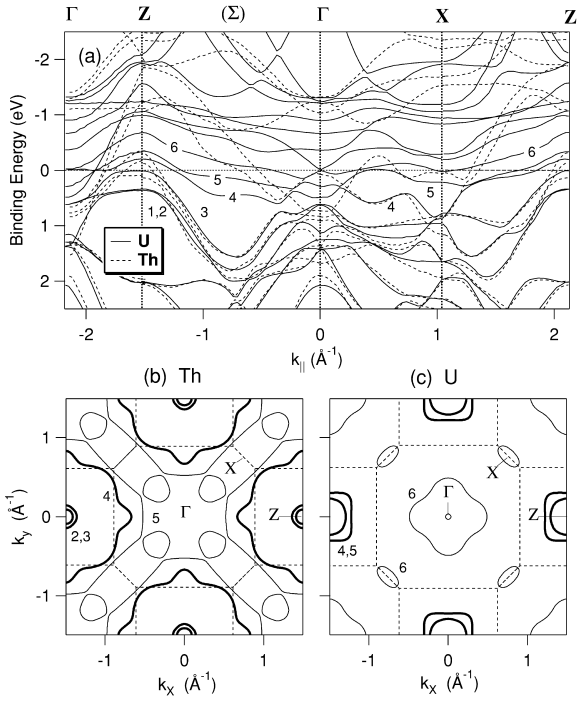

Fig. 2. Comparison of (a) theoretical LDA band structure and (b, c) 2-D Fermi-surface contours for $ThRu_2Si_2$ and URu_2Si_2. Same format as Fig. 1.

rise to other sheets of FS, the details of which vary with the material. Typically, the sheet associated with band 4 is a closed hole surface centered at Z, referred to as the ''pillow'' in Ce, and the FS sheet associated with band 5 is multiply connected. Also notable is the existence of a saddle point in the dispersion of states within 1 eV below E_F at Γ. While these bands disperse to higher binding energy in the $k_x - k_y$ plane, i.e. along Z–(Σ)–Γ and Γ–X, they disperse to lower binding energy along k_z and cross E_F approximately half way between Γ and Z. This saddle point dispersion forms a signature of the Γ-point discussed in Section 1.2 and Fig. 4.

A key difference among the different theoretical band structures is the occurrence and location of the narrow 4*f* and 5*f* bands. For the f^0 systems, the unoccupied bands are at least 3 eV above E_F. For Ce the narrow 4*f* bands are primarily confined to within 1 eV above E_F, while for U the 5*f* bandwidth is larger (≈ 2 eV) with greater overlap of the Fermi level. The larger 5*f* bandwidth relative to the 4*f* bandwidth is expected due to the larger radial extent of the 5*f* wave functions and the greater spatial overlap with other orbitals. The greater overlap of the U 5*f* bands with E_F compared to that for the Ce 4*f* bands is also due to the differing *f*-occupations.

It is important to identify the systematic effects of the changing numbers of conduction electrons and *f* electrons, both of which contribute to the FS in these calculations. The nominal configurations are La^{3+} ($4f^0$), Ce^{3+} ($4f^1$), Th^{4+} ($4f^0$), U^{4+} ($4f^2$). The changes are simple for the f^0 materials. The 4^+ valence of the Th atoms compared to the 3^+ valence of La atoms means that one extra electron is contributed to the conduction band in $ThRu_2Si_2$, thus raising the chemical potential relative to that of $LaRu_2Si_2$ and resulting in one less FS hole pocket at Z. In $LaRu_2Si_2$, the band 4 hole pocket centered at Z is very large, while band 5 crosses E_F twice, forming small electron like FS sheets near Γ. As the chemical potential is raised going from La to Th, the E_F crossing of band 4 moves towards Z and the hole-pocket shrinks to a contour roughly the size of the BZ boundary. The electron surface due to band 5 increases in size and connects to neighboring BZ's along Γ–X.

Comparisons involving changing numbers of *f*-electrons are more complex. Comparing La and Ce in Fig. 1(a), we see that the hybridization of narrow band 4*f* states above E_F with broad band states of compatible symmetry has the main effect of moving E_F-crossings already present for $LaRu_2Si_2$ and thereby changing the FS volume to accommodate the additional *f*-electron, without changing the number of E_F-crossings. The effect on the bands 1, 2 and 3 near Z is small enough that the number of small hole pockets near Z is unchanged. The large changes occur for bands 4 and 5. The large Z-point hole surface of band 4 in $LaRu_2Si_2$ shrinks considerably to become in $CeRu_2Si_2$ the square ''pillow'' hole surface nearly following the BZ contour, and the electron sheets associated with band 5 near Γ expand. One sheet expands enough to change its connectivity similar to $ThRu_2Si_2$. Thus the need to accommodate the additional *f* electron in going from La to Ce, shared roughly equally between bands 4 and 5, makes definite changes in the sizes of the FS sheets, and a continuous general variation between the two FS topologies is easily seen.

In the hybridization process, the Fermi velocities are decreased, thereby increasing the density of states at E_F. In particular band 4 has a much shallower dispersion at E_F compared to that in $LaRu_2Si_2$. Indeed, dHvA measurements of FS orbits in $CeRu_2Si_2$ [23] have identified the existence of a large FS pocket having a large effective mass that is primarily responsible for its large specific heat coefficient of 350 mJ/mol-K^2. This FS sheet is consistent with the Z-point pillow FS of band 4, providing an example of the origin of heavy mass bands with *f*-character at E_F within the LDA framework. Although the LDA pillow mass is much larger for Ce than La, it is nonetheless much smaller than the experimental value in Ce. Indeed, it is well known that the bandwidths of the 4*f* and 5*f* electrons calculated by LDA, are over-estimated by at least an order-of-magnitude and the calculated effective masses are generally too small by factors of 2–10 [5]. This large over-estimation of the bandwidth occurs because the large electron correlation energies (≈ 6 eV for Ce and ≈ 2 eV for U) are treated in only an average way in LDA calculations. Enhanced masses in agreement with experiment are obtained only by including dynamic correlation effects in some way, e.g. with the renormalized LDA discussed further below.

The comparison of $ThRu_2Si_2$ to paramagnetic URu_2Si_2 presents both a similarity and a great contrast to the comparison just made for the La and Ce systems. Similar to the change from La to Ce, there is again hybridization of the new *f* bands with bands of compatible symmetry already present in the f^0 compound. In consequence the $ThRu_2Si_2$ bands 4 and 5 are pushed even closer to the Z-point and become heavier in URu_2Si_2. However, in contrast to the situation for $CeRu_2Si_2$, the combination of larger 5*f* bandwidth and f^2 occupation results in there being entirely new bands of *f*-character dispersing downward across E_F and creating new FS sheets. One such new band (6) with a small Fermi velocity is observed along Γ–(Σ)–Z with continuation along Γ–X–Z. Also bands 1, 2 and 3 are sufficiently depressed in URu_2Si_2 that none cross E_F at the Z-point. Thus considerable disruption and discontinuous change of the FS topology from Th to U is expected within the LDA framework.

Attempts to include electron correlation within the band structure framework include non-ab initio methods of the ''LDA+U'' [33,34] and the renormalized-LDA [5]. $CeRu_2Si_2$ is regarded as a paradigm for the success of the latter method, in which the meV Kondo energy scale of the 4*f* electrons is imposed by the empirical modification of *f*-electron scattering phase shifts [5] on the FS. It is found that the topology of the LDA–FS is hardly changed, but that the resulting masses can be put in good general agreement with the dHvA masses, including the largest mass for the FS sheet of band 4, the so-called ''pillow'', mentioned above. There is then a good one to one correspondence between experiment and predictions from theory for the dHvA orbits and masses, and the large T-linear specific heat can be accounted for. The invariance of the LDA–FS in the renormalization procedure occurs frequently, but not always, as elucidated by Zwicknagl [5]. Although more sophisticated considerations are needed, the essential issue is much the same as in the discussion above for the LDA band structures, whether the FS topology is determined predominantly by the broad band E_F-crossings.

The renormalized LDA is essentially an ansatz for treating the low energy scale Kondo physics of the Anderson lattice model (or periodic Anderson model), in which there is a correlated f^n Anderson ''impurity'' at every site of a regular lattice. The impurity energetics feature an $f^n \rightarrow f^{n-1}$ ionization energy ε_f below E_F and an $f^n \rightarrow f^{n+1}$ affinity energy $-|\varepsilon_f| + U$ above E_F, where U is the on-site Coulomb repulsion energy. In the impurity model, hybridization of the *f* states to conduction band states then leads to the quenching of the *f* magnetic moment and the associated formation of the Suhl–Abrikosov or Kondo resonance at the Kondo energy $k_B T_K$ above E_F. Essentially exact solutions have been given for the ground state and spectral properties of an impurity model valid for Ce [35]. Solutions for the difficult lattice model typically set U to infinity and involve other approximations of various sorts for simplified situations that lack the real band structure aspects captured by the renormalized LDA. Only a few [6,8] of these solutions yield realistic information about the distribution of *f* spectral weight on both large and small energy scales. Nonetheless the simplest results provide important indications of

expected **k**-space dependence at generic conduction-band crossings as shown schematically in Fig. 3.

The key features in Fig. 3 for a dispersing conduction band include: (i) the renormalization of the bare *f*-level binding energy (ε_f) to a position (ε_f') just above the Fermi level, (ii) avoided crossings that form a hybridization gap and two branches (E^- and E^+) with continuous variation of *f*–*d* character mixing from the flat to the dispersing states, and (iii) a potentially great reduction of the new Fermi velocity of the E^- branch relative to the original unhybridized *d*-band velocity. The precise location of the new E_F-crossing ($\mathbf{k}_F'$) as compared to the unhybridized *d*-band $\mathbf{k}_F$, should be determined by adjustment of the chemical potential to include the *f*-electrons. At the level of Fig. 3, the renormalized *f*-level energy and the renormalized hybridization are adjustable parameters, but in a full microscopic treatment they are linked to the original Hamiltonian parameters through Kondo-like relations. The renormalized *f*-level above E_F is essentially the impurity model Kondo resonance, the Kondo energetics of which are captured in the procedure of the renormalized LDA. One sees again in this view of heavy mass formation the tendency that the basic FS topology is determined by the conduction band E_F-crossings in the absence of *f*-state hybridization, which we take in this paper to be that of the f^0 compounds.

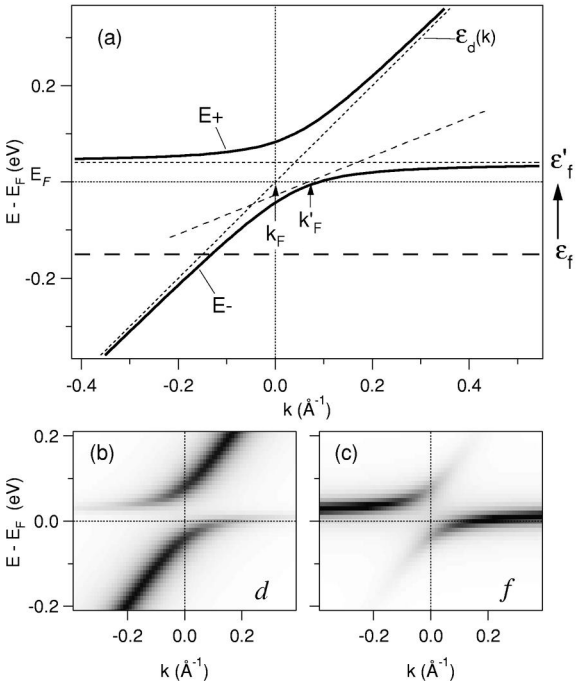

Fig. 3. (a) Schematic of the Anderson lattice model energy branches in the vicinity of a *d*-band crossing. (b, c) Spectral weight images illustrating the mixing of *f* and *d*-character along the two energy branches.

For $CeRu_2Si_2$ there is a general similarity between the Anderson lattice schematic of Fig. 3 and the comparison within the LDA to $LaRu_2Si_2$ in Fig. 1, apart from the absence of Kondo energetics which are added in the renormalized LDA. The agreement between dHvA and the LDA FS calculations in some Ce compounds has often been cited as evidence for a simple ''itinerant bands'' picture of the Ce 4*f* electrons. This notion has resulted in experimental attempts to verify the presence of narrow itinerant *f*-''bands'' by ARPES, and has been used in arguments for the (complete) failure of the single impurity model [17,18]. We see here that the success of the LDA for the FS of a Ce material can be viewed as perhaps somewhat fortuitous in that mixing with the 4*f* bands mainly changes the f^0 FS by pushing its E_F crossings to accommodate the *f*-electron. But for URu_2Si_2, where the LDA FS is very different from that of $ThRu_2Si_2$, as seen in Fig. 2, it is unclear that the expectations for the various pictures will be the same. Although dHvA data seem to be explained by LDA calculations for some heavy fermion uranium materials, e.g. UPt_3 [36,37], this is not the case for URu_2Si_2 [38,39]. The antiferromagnetic phase transition at 17.5 K in URu_2Si_2, and a possible associated change in the Fermi surface, complicates the comparison of LDA, dHvA and ARPES. Nevertheless, one can hypothesize that the difficulty for URu_2Si_2 reflects the kind of gross difference from the f^0 situation seen in the band structure comparison of Fig. 2. The experimental studies of paramagnetic URu_2Si_2 described here offer the possibility to test this hypothesis.

One other very important aspect of the correlated picture may be testable by ARPES experiments. If the low energy scale effects of hybridization can somehow be turned off, then the *f*-electrons are atomic-like with local magnetic moments. Friedel sum rule or Fermi surface sum rule arguments implying the Kondo resonance then fail. The FS should no longer count the *f*-electrons and should

revert to that of the f^0 compound. One way to accomplish this is by the full restoration of the *f*-magnetic moment, e.g. through magnetic ordering or very high magnetic fields. Indeed for $CeRu_2Si_2$ dHvA frequencies above a metamagnetic transition at ≈ 8 T change abruptly to values in closer agreement with the LDA FS of $LaRu_2Si_2$ [40]. For the ferromagnet isomorph $CeRu_2Ge_2$, dHvA frequencies are consistent with a five sheet FS [41] where the pieces from bands 4 and 5 are modified to contain one less electron per cell than for $CeRu_2Si_2$. Zwicknagl [22] has set forth the deep conjecture that, e.g. for $CeRu_2Si_2$, at temperatures far in excess of T_K where the magnetic moment is unquenched, the FS should exclude the *f*-electrons.

1.2. Experiment

The ARPES experiments were performed at two synchrotrons with three different end stations. Low photon energy (14–35 eV) experiments were performed at the Ames/Montana beamline at the SRC synchrotron with a fixed sample/moveable detector geometry and with energy and angular resolutions of $\Delta E = 50$–100 meV and $\Delta\theta = 2°$. Photons from an ERG monochromator with energies greater than 40 eV but lower resolution were also available at the SRC beamline. Samples were pre-aligned with Laue diffraction, cooled via a He refrigerator and then cleaved and measured in ultra-high vacuum ($< 4 \times 10^{-11}$ Torr) at a sample temperature of $T_s \approx 25$ K. High photon energy (80–200 eV) experiments were performed at the Advanced Light Source (ALS) undulator beamline 7.0 employing a high flux-narrow focus (100 μm) beam spot and a fixed detector/rotating sample geometry with 16-energy channel parallel detection ($\Delta E = 60$ meV and $\Delta\theta = 0.7°$). Rare-earth samples were cleaved and measured at ≤ 150 K, while radioactive actinide samples were cleaved at room temperature before being immediately transferred to a LN-cooled sample manipulator and measured, all in a vacuum typically $< 1 \times 10^{-10}$ Torr. Refined sample alignment was determined in situ by the symmetry of the Fermi-energy emission intensity maps. In addition, high resolution experiments were performed on URu_2Si_2 at the ALS Beamline 10.0 employing a flowing He cryostat, $T_s \geq 20$ K, and a Scienta 200 analyzer with $\Delta E = 20$ meV and $\Delta\theta = 0.36°$. Samples were typically measured at the ALS within a 12 h period after cleavage, while multi-day experiments were performed at the SRC.

ARPES experiments at a fixed photon energy measure along spherical arcs in **k**-space. Fig. 4 shows a schematic of these measurement arcs along with the XRu_2Si_2 bct Brillouin zones along two high symmetry directions, [100] and [110], for both low energy and high energy experiments. From basic photoemission theory, the photohole momentum (k_x) is translationally invariant parallel to the surface and is unambiguously determined by the emission angle and kinetic energy of the photoelectron [42]. Perpendicular to the surface, the relation between the photoelectron and photohole momenta (k_z) also involves the surface potential which is parametrized by an ''inner potential step'' V_0 whose value is empirically adjusted to be consistent with ARPES spectral signatures. For example, Fig. 5 shows normal emission spectra of URu_2Si_2, acquired from both synchrotrons, spanning a broad photon energy range from 14 eV to 230 eV and traversing –Γ–Z–Γ– multiple times. While these spectra tend always to show a resolution-limited peak very close to E_F, the

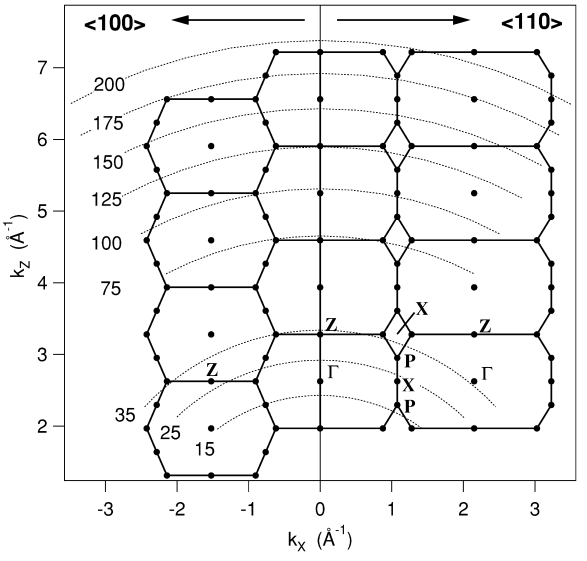

Fig. 4. Schematic of the relation between the hemispherical measurement arcs in **k**-space and the XRu_2Si_2 bct Brillouin zones for both the low energy (15–35 eV) and high-energy (75–200 eV) ARPES experiments.

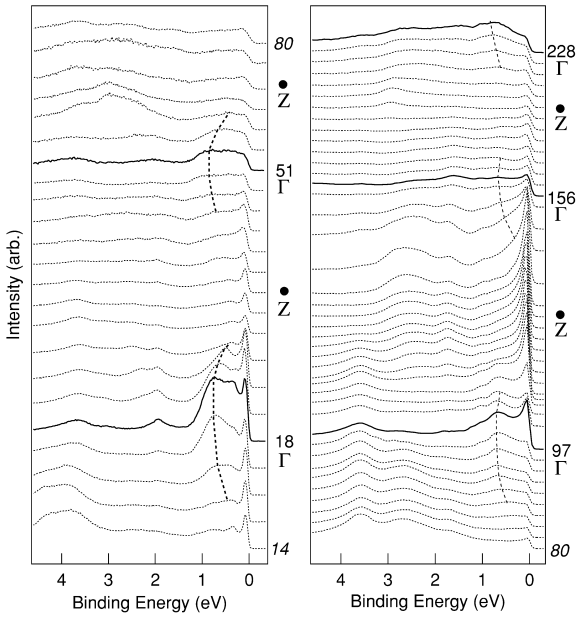

Fig. 5. Normal emission spectra of URu_2Si_2 from 14 to 228 eV. Dashed lines illustrate band dispersions signifying the Γ-points. Bullets indicate approximate spectra at Z-points.

Γ-point can be distinguished from the Z-point by an additional build up of spectral weight at ≈ 0.7 eV binding energy that corresponds to the saddle point bands discussed in Figs. 1 and 2. The electron-like dispersion is observed at 18, 51, 97, 156 and 228 eV, consistent with $V_0 = 12$ eV. Identification of Γ at 18 eV along normal emission is also consistent with Fermi surface features observed in a $k_x - k_z$ Fermi-energy intensity map (discussed below) acquired for URu_2Si_2 [21]. The spectra in Fig. 5 also highlight the well-known resonant enhancement in the valence band near E_F for URu_2Si_2 at the U $5d \rightarrow 5f$ absorption maxima of 98 and 108 eV.

Since resonant valence band photoemission measurements around 100 eV photon energy are very near the minimum of the electron escape depth, indicating extreme surface sensitivity, it is important to call attention to any bulk signatures that might be present in our ARPES data. The identification of Γ-point signatures over five Brillouin zones along normal emission and k_z-dependent FS maps is strong evidence for bulk character in the states being probed with ARPES. Additional evidence of bulk character is the favorable agreement between experimental band dispersions and the theoretical bulk band calculations (to be shown in Sections 2 and 3). For such direct comparisons to bulk band theory, suitable choices of higher photon energies, as in Fig. 4, correspond to measurement arcs that are close approximations to the high-symmetry directions of Γ–(Σ)–Z and Γ–X–Γ (or Z–X–Z). However, the theoretical band structure of the XRu_2Si_2 systems, consisting of small hole pockets at the Γ and Z points, can be very sensitive to the precise measurement arc, e.g. an arc not cutting through the center of a small ellipsoidal pocket can affect the size of the measured ellipsoidal contour or even miss the pocket and show a band maximum below E_F (no Fermi crossing). This sensitivity to k_z and the curvature of the measurement is partially alleviated by k_z-broadening [43] that arises from the finite mean free path of the electrons, resulting in some blurring of the three-dimensionality of the FS topologies. Nevertheless, when a measurement does not pass close to a high-symmetry point due to the selection of photon energy or to the k_z-curvature of the **k**-space arc, the identifying nearest high symmetry point used in the text or in the labeling of a figure is placed in quotes for clarity. For example, a measurement in the ⟨110⟩ direction at $h\nu = 154$ eV, where the arc passes directly through Γ at normal emission, very close to the X-point at the BZ boundary, and midway between Γ and Z in the second BZ, would be labeled Γ–X–''Γ''. Also, ARPES of URu_2Si_2 has been measured previously in the [110] plane using He I excitation [14] which according to Fig. 4 corresponds to Γ–''X''–''Γ''.

The Fermi-energy intensity mapping technique [44–47] monitors the photoemission intensity within a constant kinetic energy window as a function of sample or detector angle and/or photon energy. Intensity modulations highlight the passing (or close approach) of bands through this energy window which when set at the Fermi-level, identifies the **k**-space location of the approach or crossing of dispersing bands that form the Fermi-surface. Parallel detection or automated motions allow a much higher sampling density and larger range of **k**-space emission directions to be sampled than normally achievable with acquisition of individual spectra. Acquisition of these global ''FS maps'', which also provide information on sample alignment, matrix-element and polarization effects, is very useful in

instructing where to focus attention with more detailed high-resolution spectra. SRC experimental maps were acquired with semi-automation of two orthogonal angles of the detector in a fixed sample geometry. ALS Beamline 7.0 maps were acquired via automated spherical-coordinate sample rotations.

While differencing of on- and off-resonance angle-integrated valence spectra is a common procedure to isolate the *f* partial density of states, the separate on- and off-resonance FS maps for X=(Ce, U) provide separate and complementary information. On-resonance FS maps are important to understand the **k**-space distribution of *f*-states, and off-resonance FS maps are important both for the comparison of FS contours to the f^0 system as well as for the correlation of on-resonance *f*-weight to the *d*-FS contours. In addition, the assumption for such subtraction procedures, that the non-*f* cross-section variation with photon energy is minimal, is less valid for angle-resolved photoemission and for large differences in photon energy. Thus, in this paper, the on- and off-resonance FS maps are presented separately without attempts at differencing.

The atomic stacking (–X–Si–Ru–Si–X–) of the body-centered tetragonal (bct) crystal structure of the XRu_2Si_2 system makes the material very amenable to cleavage in vacuum to expose clean (001) surfaces. The bct lattice constants vary from $a=4.215$ to 4.129 Å and $c=9.930$ to 9.575 Å, with $LaRu_2Si_2$ (URu_2Si_2) having the largest (smallest) unit cell. Crystals were formed by a rapidly cooled arc-melt technique that produces mm-sized crystalline flakes of varying domain purity, i.e. high quality large rare-earth flakes and smaller mixed domain actinide flakes. In addition, float zone-refined crystals from arc-melted ingots were used for the majority of URu_2Si_2 measurements. Low energy electron diffraction was performed on selected samples after ARPES measurements and relatively sharp (unreconstructed) 1×1 patterns were exhibited in each case.

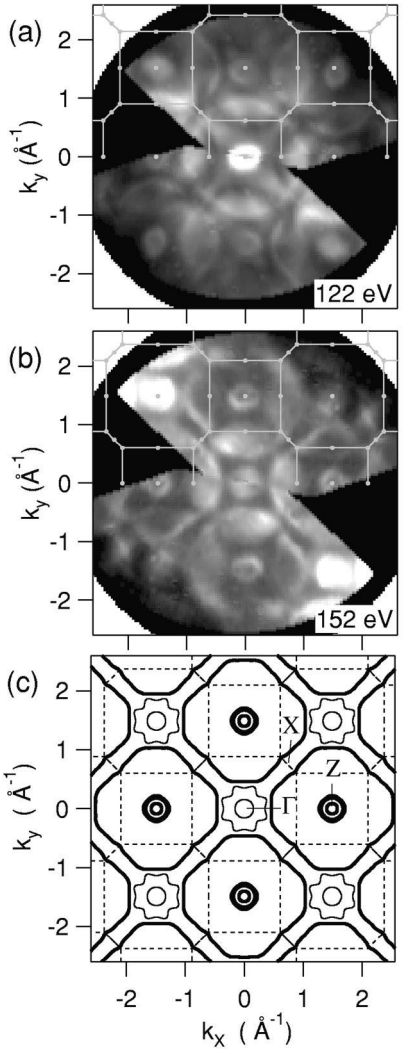

Fig. 6. Fermi-energy intensity maps of $LaRu_2Si_2$ at (a) 122 eV and (b) 152 eV. Lighter grayscale is higher E_F-intensity. (c) Theoretical contours of hole (bold) and electron (fine) Fermi surface topologies.

2. Results: X=La, Ce

2.1. $LaRu_2Si_2$

Fig. 6(a, b) shows E_F-intensity maps of $LaRu_2Si_2$ acquired at $h\nu=122$ eV and 152 eV which correspond to the Z and Γ points, respectively, at normal emission. The maps were acquired over a 120° azimuth and a 30° polar angle range, and have been corrected for misorientation of the sample surface to the sample goniometer rotation axes, two-fold symmetrized, and plotted as a projection onto the k_x-k_y plane. BCT Brillouin zone borders are overplotted in the upper half of the maps using the corresponding normal emission Z and Γ **k**-points.

Three main pieces of FS are observed to repeat in multiple Brillouin zones in the experimental maps of Fig. 6(a,b): (i, ii) small circular closed sheets centered at Γ and Z and (iii) a large sheet centered at Z that extends into the second BZ. The two maps in Fig. 6 do not distinguish the disconnectedness along k_z of the small FS pockets at Γ and Z. In fact, since Γ and Z alternately repeat along vertical k_z lines, the data could be interpreted as showing a single piece of FS that has been broadened along k_z. However, strong evidence for three-dimensionality of the FS and the existence of experimental k_z-resolution is provided by the large FS contour which is observed to shift from a Z-point center at normal emission at 122 eV to Z-point centers in the outer BZ's at 152 eV, consistent with the stacking of bct Brillouin zones in **k**-space (Fig. 3). However, similar but fainter large FS contours centered around Γ are observable and may result from the hemispherical curvature of the constant energy surfaces being measured in **k**-space and/or k_z-broadening which would give a ghost contribution from hole pockets with other Z-point centers.

A schematic of the theoretical FS contours [29] is shown in Fig. 6(c) where bold (fine) lines indicate theoretical hole (electron) Fermi surfaces. Band theory predicts (i) three concentric hole pockets centered on Z, (ii) very small electron pockets offset from and surrounding Γ and (iii) a large hole surface centered on Z whose diameter extends into the next BZ's. The qualitative agreement between the experimental maps and the theory is very good, although the experimental FS maps do not resolve the small Z point contour into three concentric pockets, nor do they distinguish the electron or hole character of the FS contours, which can be determined only from valence spectra dispersions near E_F.

Fig. 7(a) shows reverse grayscale images of $LaRu_2Si_2$ valence band spectra acquired at $h\nu = 152$ eV with 0.5° polar angle steps along two azimuth angles separated by 45° that correspond to the Γ–(Σ)–Z and Γ–X–Γ high symmetry directions. For comparison, the theoretical band structure along the same two directions is shown in Fig. 7(b). Ignoring the weaker features in the experimental data and various detailed discrepancies with theory, major agreement with theory can be identified. The Z point FS is verified experimentally to be a hole pocket that

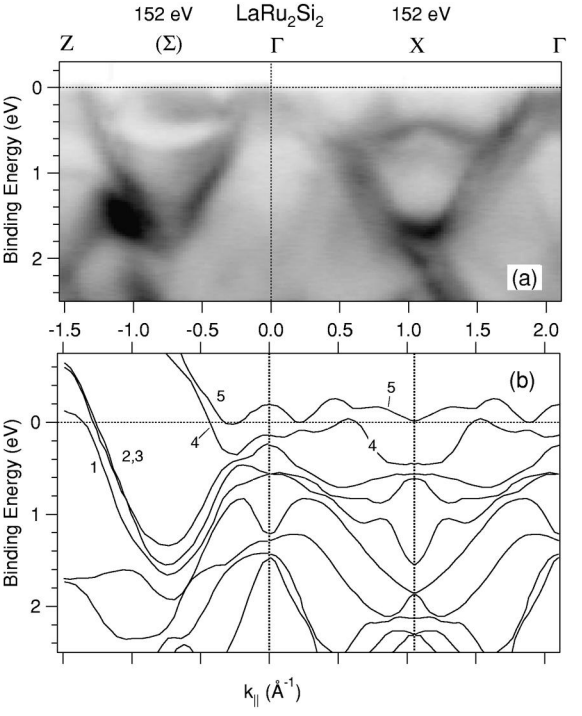

Fig. 7. (a) Valence band intensity maps of $LaRu_2Si_2$ at 152 eV along high-symmetry azimuth angles corresponding to Γ–(Σ)–"Z" and Γ–X–"Γ". Darker grayscale is higher spectral intensity. (b) Theoretical band structure calculation for $LaRu_2Si_2$.

originates from bands that disperse symmetrically along Z–(Σ)–Γ.

Band theory shows a complicated region near Γ arising from band hybridizations. A key feature, though, is the existence of a mostly unoccupied band (5) just above E_F at Γ that dips below E_F forming tiny electron pockets at $k_x \approx -0.25$ Å^{-1}. The existence of such an electron pocket is readily apparent in the experimental data along Γ–(Σ)–Z, centered at $k_x = -0.35$ Å^{-1} with 0.3 eV band minimum. However, the outer edge of the experimental electron pocket corresponds to the outer-edge of the large contour in the FS maps of Fig. 6, i.e. the contour that has the connectivity of the large hole-surface of band 4. A possible reconciliation of this discrepancy is that band 5 does not actually cross E_F while band 4 recrosses E_F before the Γ-point. This interpretation is not contradicted by dHvA data, which also show poor agreement with LDA in the magnetic field angle-dependence of the smallest frequency FS orbits

in both $LaRu_2Si_2$ [29] and $CeRu_2Ge_2$ [41], and agrees better with the valence band image in Fig. 7(a), which shows that bands (1–3) disperse very close to E_F at Γ, possibly even forming a small hole surface. Next to the small electron pocket, roughly halfway between Γ and Z, there is a fuzzy region of near-E_F weight that correlates with the ''football-shaped'' E_F intensities on the interior boundary of the large Z-point hole surfaces seen in Fig. 6 and discussed earlier in terms of k_z-broadening.

Along Γ–X–Γ we observe a dominant band dispersion that is symmetric about the X point also with a band minimum of ≈1.6 eV and a second band dispersing downwards from the X-point at ≈0.5 eV binding energy. Both of these features are present in the band theory, albeit with a greater splitting of the bands. The band theory also predicts small electron pockets (above and below) the X-point (visible only with 3D FS figures) originating from fairly flat dispersions that are probably very sensitive in size to band dispersions and location of the chemical potential. Some experimental weight at E_F near the X-point has the wrong dispersion compared to the theoretical bands, but may be related to the hypothesis concerning bands 4 and 5 in the preceding paragraph.

So far we have established the ability of ARPES to identify the basic band structure and FS topology of $LaRu_2Si_2$, and have demonstrated the basic validity of the LDA band structure calculations. Good agreement between experiment and theory is observed not only below 0.5 eV binding energy, but also in the FS region including large hole surfaces centered on Z in $LaRu_2Si_2$ and small electron pockets around Γ. The large hole surface centered on Z is the important ''pillow'' FS which is predicted to become very heavy in $CeRu_2Si_2$, as described in Section 1.2. Next we build on this agreement and understanding of the $4f^0$ system to study and identify correlation effects in the $4f^1$ system $CeRu_2Si_2$.

2.2. $CeRu_2Si_2$

This section presents ARPES information on the FS and on the global variation of the 4*f*-weight of $CeRu_2Si_2$ with clear signatures of the **k**-space locations being probed, and with a level of detail that has not been achieved previously in ARPES studies of Ce materials. Hence we are in the very beginning stages of making an interpretation of the data and we proceed with qualitative observations, looking for signatures of the theoretical models discussed in Section 1.1. We find some very interesting surprises.

Fig. 8(a) shows reverse grayscale images of $CeRu_2Si_2$ valence band spectra at 154 eV, corresponding to the Γ-point at normal emission. Comparison of this data to that of $LaRu_2Si_2$ in Fig. 7(a) shows that the two band structures below ≈0.5 eV binding energy are virtually identical including relative intensities of spectral weight. Similarly the agreement of the band structure below 0.5 eV is also very good in comparison to the LDA calculation shown in Fig. 8(b). The different relative weights at Γ at normal emission and Γ in the second BZ can result from the curvature of the **k**-space measurements arcs, i.e. the measurements cut below Γ in the second BZ. The major difference between the two systems is the presence of weight at E_F over large regions of the FS. This intensity originates from Ce

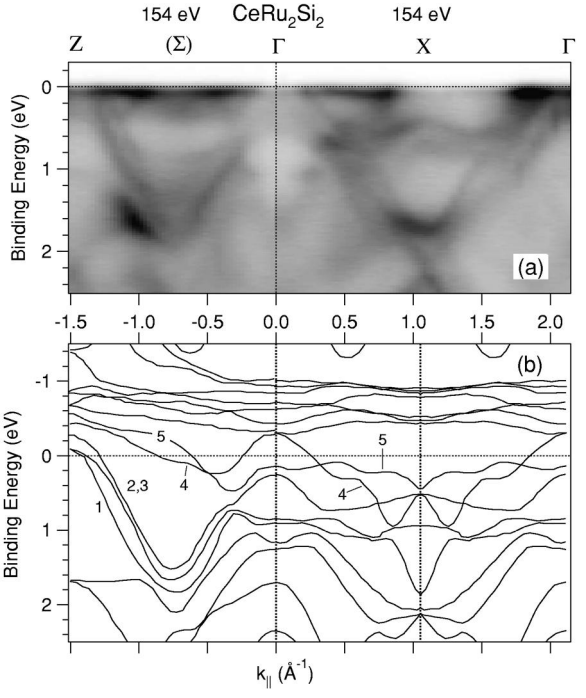

Fig. 8. (a) Valence band intensity maps of $CeRu_2Si_2$ at 154 eV along high-symmetry azimuth angles corresponding to Γ–(Σ)–''Z'' and Γ–X–''Γ''. (b) Theoretical band structure calculation for $CeRu_2Si_2$.

4*f* weight that is still relatively strong at 154 eV in spite of being 30 eV above the $4d \rightarrow 4f$ resonance at 122 eV. While this tells us something important about the 4*f* states, it obscures the details of the *d*-band FS crossings. Measurements at lower photon energy (15–35 eV, not shown here) reveal hole surfaces at both Γ and Z and a small hole-like dispersion down to 0.25 eV centered on the X-point.

To further investigate the near-E_F *d*-band structure, we turn attention to the FS map in Fig. 9(a) acquired at 91 eV, which is below the 122 eV resonance so that the 4*f* states are weaker, and which is in a region of large *d*-cross section. This map was acquired over a 220° azimuth range out to 30° polar angle and has been 4-fold symmetrized. We begin by calling attention to a weaker feature of great importance for our discussion below. Glancing back and forth between Fig. 6(b) and Fig. 9(a), initially with attention to the central BZ, reveals in 9(a) the dim pattern of a large surface centered on the second BZ Z-points and extending into the central BZ, very similar to the one in $LaRu_2Si_2$. The pairs of straight segments of intensity on either side of the X-points are parts of such large pieces of FS. One also sees some of the additional intensity ascribed in Fig. 6(b) to k_z-broadening of this large FS piece. Other clearly observable features include (i) a bright intensity at the normal emission Γ-point, (ii) an intense closed contour in the second BZ's that correspond to near Γ-points, (iii) weak intensity and possibly small closed topologies around the Z-points.

Fig. 9(c) shows calculated 2D FS contours for $CeRu_2Si_2$. The existence of small closed contours at the Γ and Z-points is in qualitative agreement with the image of Fig. 9(a). At first glance their similar sizes and shapes tempt one to associate the large Z-point contour in experiment with the large Z-point electron contour in theory. Apparently absent in this association is the pillow hole FS contour that closely follows the square BZ boundary centered on Z, important because it corresponds to the major heavy mass band identified by dHvA studies in accordance with renormalized LDA theory. Further consideration of the data suggests the reverse interpretation, that the theoretical electron surface is not observed and that the band 4 hole FS does appear in the data, but with the larger surface appropriate to the La compound (Fig. 6(c)) rather than the smaller one of the

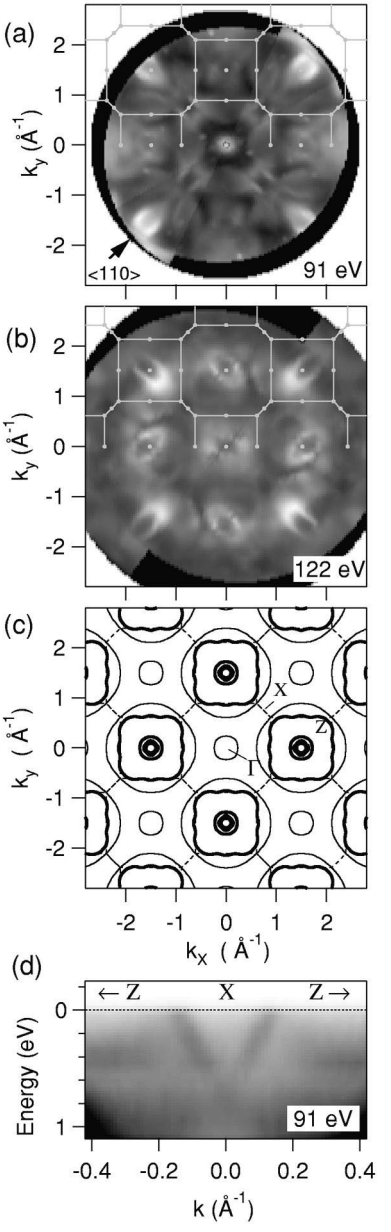

Fig. 9. Off- and on-resonance Fermi-energy intensity maps of $CeRu_2Si_2$ at (a) 91 eV and (b) 122 eV. (c) Theoretical contours of hole (bold) and electron (fine) Fermi surface topologies. (d) Valence band dispersion at the X-point at 91 eV orthogonal to Γ–X (reverse grayscale).

Ce compound. Strong support for this conclusion is provided by the great overall similarity of the experimental data for La and Ce, and by the spectra

of Fig. 9(d) showing the dispersions that define the large surface near the X-point along the Z–X–Z direction. The spectra clearly show a single hole band (relative to Z) on each side of the X-point, as is appropriate for the single larger hole surface of the La compound, whereas one would observe two bands and two FS crossings for the adjacent hole and electron surfaces predicted for the Ce compound (see also Fig. 1(a)). Equivalent spectra for the La compound are very similar in showing the single band.

The surprising finding is that, in contrast to dHvA results, we observe a FS that is essentially the same as that of the La compound, i.e. that excludes the Ce 4*f* electrons. As a hypothesis for understanding this result we recall from Section 1.1 the conjecture [22] that such may be the case for $T \gg T_K$ and we take note that the temperature of these measurements is six to seven times that of $T_K \approx 20$ K, whereas the dHvA data are taken for low T (< 3 K) in the Fermi liquid regime. It is then very interesting to tune the photon energy to the $4d \rightarrow 4f$ resonance and observe the **k**-space locations of the 4*f* weight. Fig. 9(b) shows an on-resonance FS map of mostly 4*f*-character for $CeRu_2Si_2$ acquired at 122 eV (corresponding to the Z-point at normal emission). Essentially no 4*f* weight is observed for the large Z-point 4*f* hole surface. This finding is certainly consistent with our hypothesis. However we should also recall that in the Anderson impurity model the portion of the 4*f* weight below E_F that is directly associated with the low energy scale of the Kondo resonance is in any case very small.

The 4*f*-weight occurs at the elliptical contours centered on the Γ and Z points. The dHvA and renormalized LDA masses of the FS at these points are not greatly enhanced and the FS volume does not have a large contribution for the 4*f* electrons. Thus the finding of 4*f* weight may not be inconsistent with the high temperature of the measurements. We note the peculiarity that, while the major-axes of the Z-point elliptical contours are radial at normal emission, the contours centered on Γ have a 45° rotation of the major elliptical axis that breaks mirror symmetry about the ⟨100⟩ plane. For this reason the map in Fig. 9(b) has only been 2-fold symmetrized. This symmetry breaking is possibly due to a polarization selection rule effect related to the detection geometry that contains the polar rotation axis in the plane of the linearly-polarized photon electric-field vector. Further studies are warranted to investigate the true origin of this behavior. In general, the 4*f*-character ellipses have a size and shape that closely match the strongest *d*-character contours in Fig. 9(a). This gives an overall impression of *f*-weight having a very close correspondence to the locations of the off-resonance *d*-band FS, except for the large hole pocket of band 4.

Another important view of the 4*f*-weight variation near E_F in $CeRu_2Si_2$ is given by the valence band spectra for off- and on-resonance photon energies. Fig. 10 shows a polar angle variation of valence spectra along the ⟨110⟩ azimuth corresponding to the Γ–X–Γ at 154 eV and Z–X–Z at 122 eV. The above-resonance VB map of Fig. 8(a) along ⟨110⟩ is a subset of the spectra in Fig. 10(a) and a 45° diagonal in the on-resonance FS map image of Fig. 9(b) corresponds to the spectra in Fig. 10(b). The spectra are acquired with 0.5° angular steps ($\Delta k \approx 0.05$ Å^{-1}) and high-symmetry spectra are labeled and indicated by bold lines. An incremental energy shift has been applied to provide a better visual perspective of the large weight variation at E_F. What

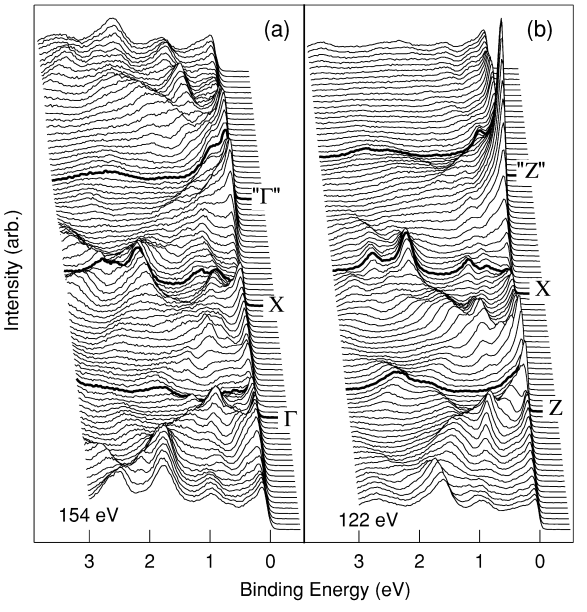

Fig. 10. Off- and on-resonance valence band spectra of $CeRu_2Si_2$ at (a) 154 eV and (b) 122 eV along the ⟨110⟩ direction showing the large 4*f* spectral weight variations near E_F.

we observe in Fig. 10(a), where the Ce 4*f* cross section is still relatively strong, is a persistence of a peak impinging on E_F throughout most of the spectra with the exception of the X-point. On-resonance Ce 4*f* weight in Fig. 10(b) becomes especially enhanced at points near the normal emission Z-point with a clear correspondence to the locations of the E_F crossings of a hole-like *d*-band. In addition, a gigantic enhancement of the Ce 4*f* weight is observed at one side of the Z-point in the second BZ. The amplitude of this *f*-weight makes it difficult to discern a similar connection to a weaker amplitude *d*-band E_F-crossing. However, the correspondence of this strong peak to a distinct elliptical FS contour feature in the FS map of Fig. 9(b) is evidence that there does exist a *d*-band crossing associated with this *f*-weight.

We note further that while the E_F peak in Fig. 10 exhibits dramatic intensity variations as a function of angle, there is no distinct dispersion of spectral weight away from E_F with one notable exception of the E_F crossing of a distinct *d*-band hole pocket centered on the Z-point. This location represents a fairly isolated region with 4*f* hybridization to a *d*-band and hence the observed dispersion can immediately be speculated to be the result of mixing of *f* and *d*-character states. The spectral lineshapes of *f*–*d* mixing in a Ce compound have not been presented before in the literature. This fairly idealized *f*–*d* mixing region at the Z-point is discussed in more detail in Section 3.1 with comparison to observations for URu_2Si_2 that are presented in the next section.

3. Results: X = Th, U

In this section we present a comparison of the data for the actinide systems containing $5f^0$ thorium and $\sim 5f^2$ uranium.

3.1. $ThRu_2Si_2$

The crystalline quality, domain size and purity of orientation of $ThRu_2Si_2$ samples currently available is considerably less than for $LaRu_2Si_2$. In particular, Laue diffraction patterns of the $ThRu_2Si_2$ samples typically exhibited multiple domains with one domain dominant. While the surface sensitivity of photoemission allows measurement of a single domain in the perpendicular direction, the lateral domain size was too small to obtain high quality ARPES data on $ThRu_2Si_2$ in the rotating sample/fixed detector geometry at the ALS where the beam spot inherently moves on the sample surface. In addition, sample alignment for the fixed sample/moveable detector geometry at the SRC was further complicated by differences in orientation of the Laue patterns before and after cleavage, indicating domain inhomogeneity as a function of depth. The result was that FS maps at the SRC were a necessary ingredient to determine the sample orientation and hence to know where to acquire spectra. The results in this section are shown only for low photon energies (≤ 35 eV).

Since $ThRu_2Si_2$ is an f^0 metal similar to $LaRu_2Si_2$, we expect a very similar band structure and FS topology with differences related primarily to the different Th^{4+} and La^{3+} valences as discussed in Section 1.1. Fig. 11(a, b) shows a FS map of $ThRu_2Si_2$ acquired at 17 eV and 30 eV and projected onto the $k_x - k_y$ plane with correction to the sample orientation. No symmetrization is performed on the maps about the vertical k_y axis due to X-ray polarization effects, while a single reflection of the data is performed for angles above and below the horizontal plane of polarization ($k_y \rightarrow -k_y$). Similar to $LaRu_2Si_2$ small FS pockets are observed at the Γ and Z points. The more severe curvature of the hemispherical measurement surface at low photon energy, causes the 17 eV FS map to cut through Γ at normal emission, but then pass intermediate between Γ and Z in the second BZ (see Fig. 4). Similarly at 30 eV, normal emission cuts intermediate between Γ and Z while larger angles pass directly through the second BZ Z-point. The relative intensities at the points labeled Γ and Z in Fig. 11(a,b) between the 17 and 30 eV FS maps confirms this 3-dimensionality of the Fermi surface.

Different from $LaRu_2Si_2$, however, are distinct FS structures around the X point. Lack of observation of the large FS centered on Z compared to $LaRu_2Si_2$ (Fig. 5) could be due to the more restricted **k**-space range or to photon energy differences. Fig. 11(c) shows the theoretical FS contours of $ThRu_2Si_2$. Apart from the FS pockets at Z there does not appear to be much agreement between the experimental FS

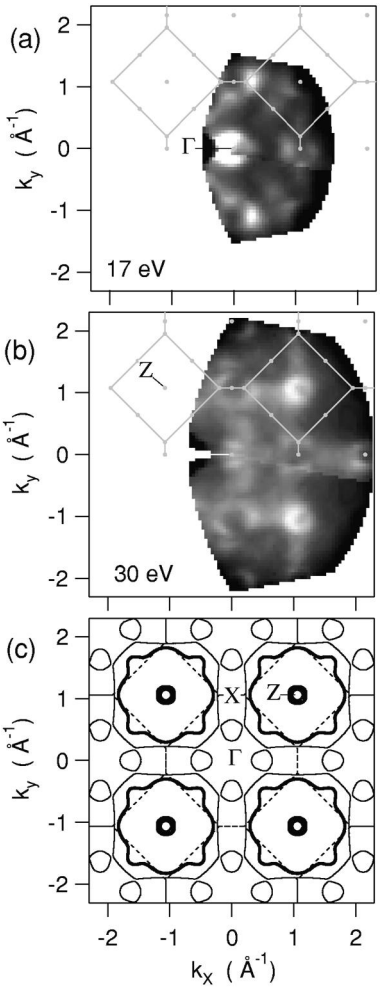

Fig. 11. Fermi-energy intensity maps of $ThRu_2Si_2$ at (a) 17 eV and (b) 30 eV. (c) Theoretical contours of hole (bold) and electron (fine) Fermi surface topologies.

map and theory. However, if we compare the band dispersions in Fig. 12, much better agreement is observed. In Fig. 12(a) we observe a parabolic dispersion along Γ–(Σ)–Z similar to the one in $LaRu_2Si_2$ that forms a hole-pocket at Z. Different, though, from $LaRu_2Si_2$, is that one band approaching Z does not reach E_F and has a band maximum at ≈0.4 eV binding energy. This observation is consistent with Th having a valence of 4^+ and the chemical potential being higher relative to $LaRu_2Si_2$.

Also in Fig. 12, along Γ–X–Γ we observe general qualitative agreement in the bands from 0.5 to 2.0 eV

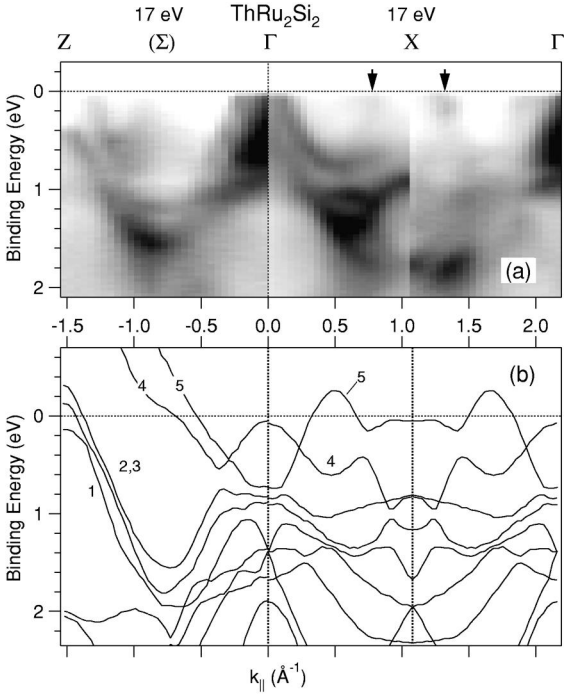

Fig. 12. (a) Valence band intensity maps of $ThRu_2Si_2$ at 17 eV along high-symmetry azimuth angles corresponding to Γ–(Σ)–"Z" and Γ–X–"Γ". Arrows indicate the location of small electron pockets. (b) Theoretical band structure calculation for $ThRu_2Si_2$.

binding energy. In addition, on both sides of the X-point we observe weight near E_F that is experimentally determined (data not shown) to be small electron pockets unresolved in Fig. 12(a). The general location of these pockets agree quite well with the theoretical band 5 which disperses below E_F at $k_{||} \approx 0.65$ Å^{-1} but does not quite cross E_F again near the X-point, as would be needed to produce small electron pockets. Hence this lack of recrossing E_F will produce a large deviation in comparison of FS contours, but the EDC's show better general agreement for this band. Overall we conclude for $ThRu_2Si_2$ that agreement with band theory is relatively good.

3.2. URu_2Si_2

Fig. 13(a) presents reverse grayscale images of URu_2Si_2 valence band spectra along two high-symmetry azimuths at two different off-resonance photon

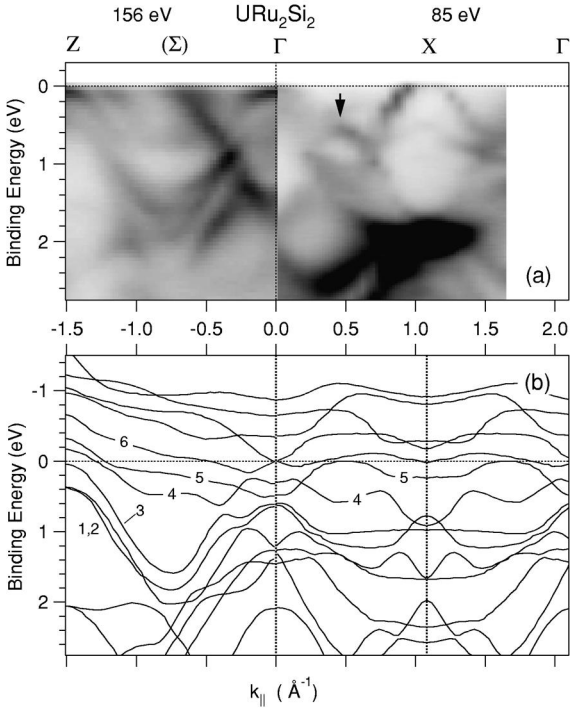

Fig. 13. (a) Valence band intensity maps of URu_2Si_2 at 156 and 85 eV along high-symmetry azimuth angles corresponding to Γ–(Σ)–"Z" and Γ–X–"Γ". The arrow indicates a possible U *d*-band discussed in the text. (b) Theoretical band structure calculation for URu_2Si_2.

energies. The residual *f*-weight far above-resonance at 156 eV is evident near E_F in contrast to the near complete suppression of *f*-weight and strong *d*-cross section below 1.5 eV observed for the 85 eV data. Comparison to the other XRu_2Si_2 band structures and to the LDA calculations in Fig. 13(b) show again the common features of a parabolic-like band dispersions with band minima at ≈1.6 eV binding energy and symmetry around the X-point and midway between Γ and Z. Also at the Z-point, band maxima at ≈0.5 eV and ≈0 eV are observed in agreement with bands (1,2) and 3, respectively, in the LDA calculation. Spectral intensity near E_F just adjacent to the Z-point along Z–(Σ)–Γ has a possible correspondence to bands 4 and/or 5.

However, in contrast to the other XRu_2Si_2 systems, the experimental bands in Fig. 13(a) also reveal quite strong disagreements with the LDA calculation in the near-E_F region where experimental dispersions down to below 1 eV have no correspondence to theory. At 156 eV, the Γ–(Σ)–Z data show a strong electron-like dispersion centered on Γ that crosses E_F close to the midpoint between Γ and Z. This band dispersion can be traced all the way to ≈1.5 eV binding energy at the Γ-point. Its presence is also evident at lower photon energies with weaker relative intensity and it serves as an additional signature that distinguishes the Γ and Z points. Along Γ–X–Γ, a data set from 85 eV is chosen to highlight a second anomaly relative to the LDA calculation, i.e. the presence of a distinct hole pocket centered on the "X"-point. This band dispersion can be traced to below 0.5 eV and has no clear theoretical counterpart in the URu_2Si_2 band calculations that predict the possible presence of a small electron-like pocket arising from a shallow dispersing band of *f*-character that dips below E_F.

Another view of this "X"-point discrepancy is in the comparison of an experimental E_F intensity map at 85 eV in Fig. 14(a), with the theoretical FS contours in Fig. 14(c). The off-resonance FS map was acquired over a 80° azimuth range and 35° polar angle and has been 4-fold symmetrized. It exhibits intensity maxima surrounding the high symmetry $k_{\|}$ locations suggestive of closed FS contours. Since the actual hemispherical measurement surface probes midway between Z and Γ along normal emission, a bct BZ centered on Z is overplotted on the FS map to reflect the fact that the measurement surface cuts close to Γ along ⟨100⟩ and close to Z along ⟨110⟩ in the second BZ's. At $k_{\|}$ corresponding to the X-points, a squarish closed contour is nicely observed to additionally repeat near the outer edge of the FS map at the boundary between the second and third radial BZ's. All three of these relatively small FS contours at Γ, Z, and X originate from hole-like dispersions as shown in Fig. 13. In contrast, the theoretical FS contours, Fig. 14(c), show significantly larger hole pockets at the Γ-point and small electron pockets at the X-point.

The reason for these large discrepancies with LDA theory has already been speculated in Section 1.1 as due to the over-estimation of the 5*f* band width which produces *f*-bands that disperse too strongly and cause unrealistic disruptions of the *d*-band FS. With this concept in mind we try to deduce the origin of the URu_2Si_2 X-point hole-pocket by look-

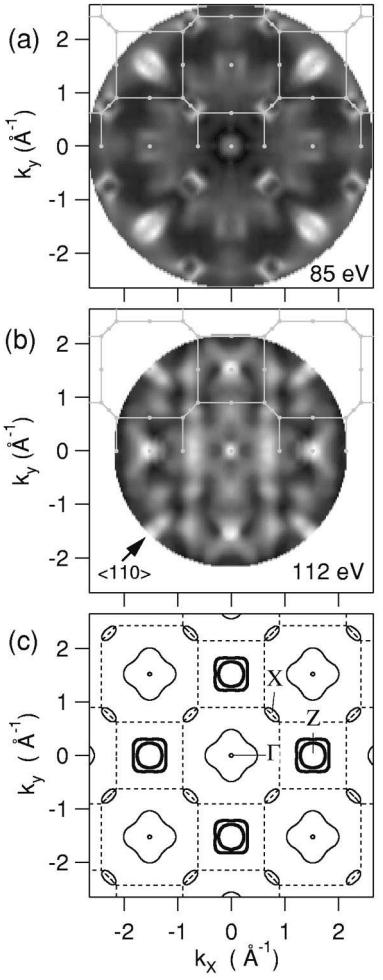

Fig. 14. Off- and on-resonance Fermi-energy intensity maps of URu_2Si_2 at (a) 85 eV and (b) 112 eV. (c) Theoretical contours of hole (bold) and electron (fine) Fermi surface topologies.

ing at the $5f^0$ $ThRu_2Si_2$ band structure (Fig. 12), where small electron pockets on either side of the X-point were found experimentally and could be consistent with a slightly modified LDA band 5. The dispersions of bands 4 and 5 near X appear to originate from the crossing-point hybridization between a parabolic electron-like band of Th *d*-character and a hole-like band of Ru *d*-character, both symmetric about the X-point. The resulting gap at the crossing point (≈ 0.3 eV) splits the two bands into two branches with the upper branch being band 5 near X. We now visualize the U 5*f* states as being more like the very narrow states of the Anderson lattice schematic of Fig. 3 than like the LDA 5*f* bands. We then speculate that for URu_2Si_2, the presence of such U 5*f* states, in addition to creating a very narrow band of states just above E_F, pushes the U-*d* electron-like band to lower energy (perhaps completely below E_F with correspondence to the arrow in Fig. 13(a)). The result is that the U-*d* and Ru-*d* crossing point is also moved to lower energy, thereby allowing the X-point Ru-*d* hole-pocket to remain as the unhybridized continuation of band 4 above E_F. Similarly, and perhaps more simply, a possible correspondence can be made between the anomalous electron-like dispersion centered at Γ in URu_2Si_2, which is particularly strong at 156 eV along Γ–(Σ)–Z, and bands 4 and/or 5 in the $5f^0$ LDA band structure of $ThRu_2Si_2$.

Next we compare the *d*-character off-resonance FS map of URu_2Si_2 to an on-resonance FS map in Fig. 14(b) acquired at 112 eV where U 5*f* character is enhanced. The data was acquired over 120° azimuth and 35° polar angle ranges and has also been 4-fold symmetrized. Similar to Fig. 14(a), normal emission of this map probes midway between Γ and Z and the overplotted BZ boundary centered on Γ reflects the $k_\parallel$ measurement points in the second BZs. Despite this measurement surface complication, we can immediately make the qualitative observation of the lack of appearance of closed FS contours. Rather, the FS map gives the impression of points of U 5*f* weight mostly at high symmetry points. Additional intensity midway from ''Z'' to ''Γ'' corresponds to the large electron-like band dispersion shown in Fig. 13. Its contour is suggestive of a larger closed surface but is not conclusive. Apart from this FS *f*-weight, the dominant on-resonance *f*-weight can be described as being confined to the interior of the off-resonance *d*-character hole-pockets.

A spectral function view of this off/on-resonance behavior is shown in Fig. 15 measured along the diagonal ⟨110⟩ direction at the same photon energies as the FS maps. Similar to Fig. 10 for $CeRu_2Si_2$, the spectra were acquired with 0.5° polar angle increments and a shift of the energy axis has been applied to better visualize the amplitude modulations near E_F. At normal emission, a hole-like dispersion, but not necessarily an E_F-crossing, is observed to strongly resonate and corresponds to the weak and strong

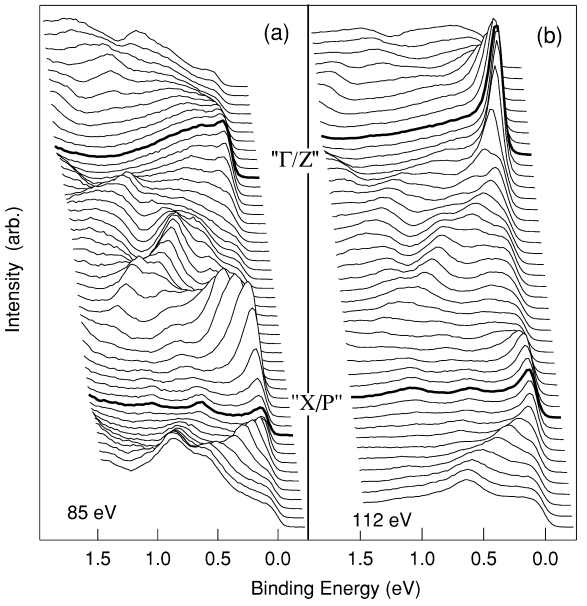

Fig. 15. Off- and on-resonance valence band spectra of URu_2Si_2 at (a) 85 eV and (b) 112 eV along the ⟨110⟩ direction showing the large 5*f* spectral weight variations near E_F.

points of intensity at the center of the FS maps in Fig. 14(a) and (b). At 112 eV, the spectra near normal emission reveal the presence of a second distinct hole-like dispersion that appears to cross E_F just outside of the strongly resonating weight at normal emission. At low photon energy, normal emission spectra of URu_2Si_2 at Γ at 18 eV reveal a finite binding energy peak with ≈50 meV gap relative to E_F, consistent with He I ARPES measurements [14].

At the diagonal BZ edge, labeled ''X/P'', a hole-pocket band dispersion is observed to significantly decrease in amplitude from 85 to 112 eV, while a weak E_F peak at the center of the pocket is observed to increase in amplitude. The reduction in amplitude of the dispersing band arises from the decreasing *d*-cross section with increasing photon energy. Also, the amplitude of the *f*-character resonance at the interior of the hole-pocket is approximately 1/3 the height of the resonance at normal emission. Also significant is that the on-resonance spectra reveal the near-complete absence of any *f*-weight resonance between the ''Γ'' and ''X'' points. We focus closer attention in Section 4.1 on this ''X''-point hole pocket in URu_2Si_2 to further elucidate and discuss the global behavior of *f*-weight confinement to the interior of the *d*-band FS hole-pockets.

4. *f* Spectral weight

4.1. f–d mixing

The isolated *d*-band hole-pocket at the ''X''-point in URu_2Si_2 presents a near ideal situation for the study of *f*- and *d*-state mixing using resonant photoemission. The FS at the ''X''-point as a function of $k_\parallel$ appears to be a squarish closed-orbit topology, in contrast to $CeRu_2Si_2$ where the near-X-point intensity derives from parallel edges of large FS contours centered on Z-points at different k_z locations. The URu_2Si_2 ''X''-point FS topology has also been probed with FS mapping as a function of photon energy [21], revealing a vertical tube of E_F intensity, i.e. no closure of the FS along the central P–X–P line. This is immediately suggestive of either a surface state or strong k_z-broadening. However, a third possibility is that it is a bulk feature with origins traceable to the $ThRu_2Si_2$ bulk band structure (as just discussed) and that very little dispersion occurs along the P–X–P direction. Indeed, because the k_z periodicity along P–X–P is half of that along Γ–Z–Γ (see Fig. 4), much less dispersion is calculated along P–X–P for all four compounds. Experimentally, the ''X''-point pocket is as robust a spectral feature to sample surface ''aging'' as other parts of the BZ, thus suggesting that it is not a surface state.

This observed two-dimensionality of the ''X''-point FS works in our favor in attempts to make direct comparison of off- and on-resonance spectra in simple terms of changing *f* and *d* cross-sections. However, it is still a valid concern that different parts of the BZ are being probed at 85 eV and 112 eV in Fig. 15. The **k**-space guide in Fig. 4 tells us that these two photon energies actually arc through similar parts of the BZ (closer to ''P''-points) below and above an X-point at ≈102 eV. In Fig. 16, off- and on-resonance spectra at the ''X''-point are presented for a smaller difference in photon energy (102 and 108 eV), higher resolution ($\Delta E \approx 40$ meV, $\Delta\theta \approx 0.2°$) and a sample temperature of 100 K.

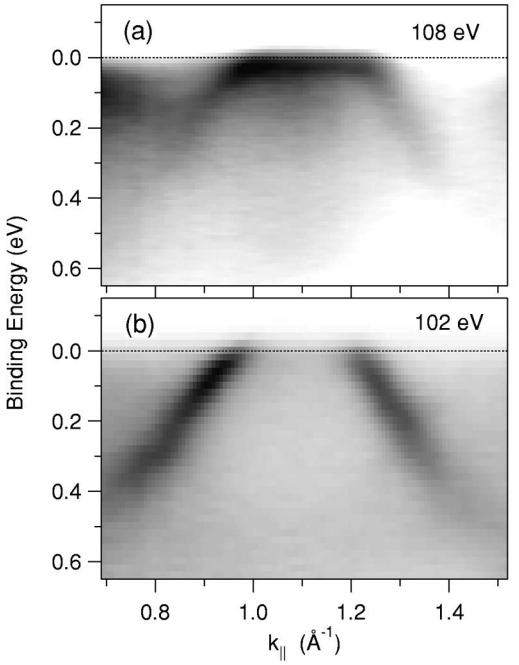

Fig. 16. Off- and on-resonance valence band structure at the X-point of URu_2Si_2 at (a) 102 eV and (b) 108 eV at 100 K. Darker grayscale is higher spectral intensity.

Similar to Fig. 15, the confinement of U 5*f* weight to the interior of the *d*-band hole pocket is quite striking in appearance, and at this resolution shows no dispersion away from the *d*-band crossings.

This **k**-space distribution of *f*-weight is a key signature of the Anderson lattice model, i.e. that ''*f*-dispersion'' occurs only through hybridization to dispersing *s–p–d* states. In the vicinity of a *d*-band E_F-crossing, the lattice model, with suitable mathematical transformation [6,7], is formally equivalent to the two-band mixing model of a dispersionless effective *f* level hybridizing with a free-electron band dispersion with renormalized hybridization (V'). As illustrated in Fig. 3, this hybridization at the *f* and *d* crossing point above E_F creates a small energy gap at the renormalized *f*-energy (ε_f') and forms two energy branches E^+ and E^- with continuous variation of *f–d* character. The gap pushes *f*-weight further above (below) ε_f' on the occupied (unoccupied) side of the *d*-band dispersion and hence further away from (towards) E_F. Thus, an ARPES experiment is expected to measure an enhancement of *f*-weight on the unoccupied side of the *d*-band dispersion, e.g. at the interior of a hole-pocket.

The relative enhancement of *f*-weight between the interior and exterior of a hole-pocket is sensitive to the values of ε_f' and V'. To illustrate this we compare in Fig. 17 on-resonance valence spectra from the ''X''-point crossing in URu_2Si_2 to a similar idealized crossing point at the normal emission Z-point hole-pocket at 122 eV in $CeRu_2Si_2$. While the URu_2Si_2 spectra in Fig. 17(a) exhibit a complete lack of *f*-weight outside the hole-pocket and uniform intensity interior to the hole-pocket, the $CeRu_2Si_2$ spectra present a different behavior. Instead an *f*-character peak at E_F is visible with approximately equal intensity both interior and exterior to the Z hole-pocket. Only close to the *d*-band E_F crossing point do we observe a small suppression and then enhancement of *f*-weight just before and after the E_F-crossing. This difference between $CeRu_2Si_2$ and URu_2Si_2 can be qualitatively understood to result from different renormalized parameters (ε_f' and V') consistent with the different bulk heavy fermion properties of the two systems. $CeRu_2Si_2$, the heavier of the two systems with a *T*-linear specific heat coefficient twice as large as that of URu_2Si_2, is

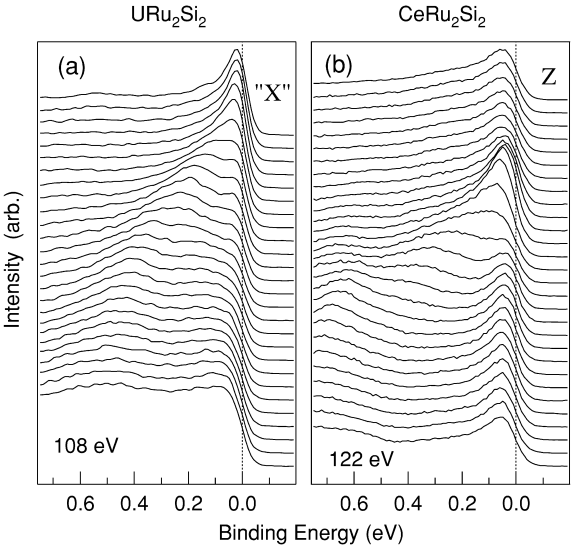

Fig. 17. High resolution on-resonance spectra near a *d*-band E_F-crossing for (a) URu_2Si_2 near the X-point and (b) $CeRu_2Si_2$ near the Z-point. Spectra are acquired with 0.25° steps ($\Delta k \approx 0.024$ Å^{-1}).

expected to have a weaker hybridization (V') and a smaller centroid f-energy (ε_f') above E_F. The persistence of Ce 4f weight throughout most of the BZ in Fig. 10(b) and Fig. 17(b) indicates that ε_f' is within a Fermi-function half-width of E_F at the sample temperature (≈ 120 K) of the ARPES measurements. Also the weaker hybridization in $CeRu_2Si_2$ is evident from the f-weight enhancement occurring only near the d-band crossing and not throughout the full interior of the Z hole-pocket. In contrast, for URu_2Si_2, ε_f' is large enough to be outside the temperature-dependent Fermi-function energy scale, yet the hybridization is strong enough to push U 5f weight close to E_F throughout the entire center of the X-point hole-pocket. This tension between ε_f' and V' in determining the f-spectral weight has the potential to be used as a tool for quantitative analysis of these parameters. Theoretical simulations within a simple two-band model can nicely reproduce the basic spectral features in Fig. 17. Such lineshape analysis will be presented elsewhere.

As discussed in Section 1.1, the reduction of Fermi-velocities and formation of heavy bands within the Anderson lattice model is also evident in the renormalized two-band approximation. Lineshape analysis of low temperature high-resolution spectra has the potential to identify and quantify such effective mass increase near E_F even if not visible by direct inspection The spectra in Fig. 17 for both $CeRu_2Si_2$ and URu_2Si_2 show small hints of such slope-reduction near E_F. We should also note that these two idealized **k**-space locations are expected to only exhibit modest mass enhancements ($m^*/m < 10$). It is other sheets of FS, such as the $CeRu_2Si_2$ ''pillow'' that have been identified by dHvA and renormalized LDA to possess the very large effective mass of greater than 100.

Also we should point out that the two idealized f–d crossing points shown in Fig. 17 do not represent the regions in **k**-space of strongest f-spectral weight. Figs. 9(b) and 14(b) show much stronger f-weight at the second BZ 122 eV ''Z''-point in $CeRu_2Si_2$ and at normal emission at 112 eV in URu_2Si_2. These large variations in f-weight ARPES intensity can result from different topologies (FS surface sizes and bare E_F velocities) of the underlying d-band as well as from matrix element effects. The finite binding energy of the near-E_F peak at Γ in URu_2Si_2, discussed earlier, suggests that the larger f-enhancement at normal emission compared to the ''X''-point is due to f–d hybridization pulling the effective f-level *below* E_F. It is not likely that a single set of renormalized parameters (ε_f' and V') with merely different d-band dispersions is adequate to describe this large f-weight variation at different points of the BZ. It is an interesting theoretical challenge to see how averaging of a ''**k**-dependent hybridization'' can produce a single energy scale which adequately describes the global bulk thermodynamic properties. The renormalized LDA is essentially a single parameter theory having this character [22], but it is not realistic for the addressing the f-spectral weight issues.

4.2. Temperature dependence

An important aspect of the Anderson single impurity and lattice models is the temperature dependence of the Kondo peak as the system is cooled below the Kondo temperature. Predictions for lattice models exist [8], but thus far the models are not realistic as to degeneracy or conduction electron number for Ce, Yb or U [48]. For the impurity model below T_K a sharpening or increase of the **k**-integrated photoemission f-spectral weight is expected for Ce and Yb, with differences originating from the one f-electron and one f-hole character, respectively [35]. Such temperature dependence has been reported for Ce [19] and Yb [49] compounds, but also disputed [18,50]. Experimentally no significant temperature variation in photoemission has yet been reported for any U compound [18]. URu_2Si_2, with an intermediate Kondo temperature of ≈ 70 K [51], is favorable for such a temperature-dependent study of the f-weight at different locations in **k**-space. The X-point was chosen for its idealized electronic structure of an isolated d-band hole pocket hybridizing with U 5f states, and for the relative absence of d-states below E_F at the center of the hole pocket.

Fig. 18 shows such angular-resolved spectra from the center of the X-point measured at resonance (108 eV) for temperatures in the experimental sequence of 100 K, 50 K and 25 K. A striking temperature dependent enhancement of the E_F peak is observed for lower temperatures. The increase from 100 K to

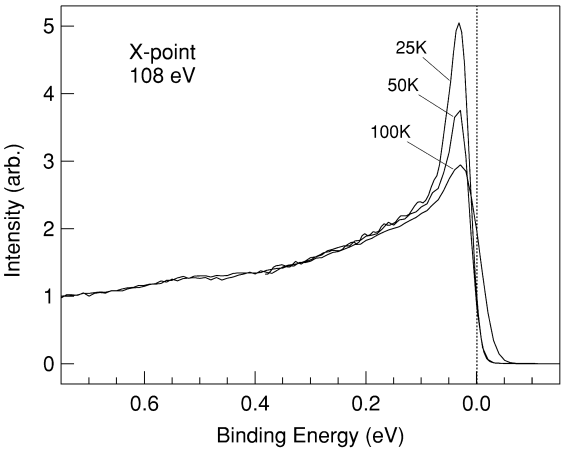

Fig. 18. Temperature dependence of angle-resolved valence spectra at 108 eV for URu_2Si_2 at the center of the ''X''-point hole-pocket.

25 K is almost a factor of two in the raw data without consideration of a temperature-invariant inelastic background (and greater than 400% with subtraction of this background). This large temperature variation is consistent with observations by point-contact spectroscopy of a resonance at E_F appearing below 60 K [52] and is interpreted as possible evidence for the Kondo singlet condensation. Previously no significant temperature variation of angle-integrated valence spectra from scraped single crystals of URu_2Si_2 [53] was observed. A more complete analysis of this Kondo-like temperature dependence in URu_2Si_2 will be presented elsewhere.

4.3. Surface effects

Surface effects in photoemission of *f*-electron systems need to be taken seriously. For Ce compounds there is a sizable body of literature with discussion of surface effects in terms of increased 4*f* binding energy and reduced *f*-hybridization resulting from smaller near-neighbor coordination at the surface [54,55]. Angle-integrated Ce valence spectra exhibit three main features: (i) a broad $f^1 \rightarrow f^0$ electron removal peak at ≈ 2 eV, (ii) a Kondo resonance spin–orbit sideband at ≈ 0.3 eV and (iii) a narrow peak impinging on E_F corresponding to the occupied tail of the Kondo resonance. The reduced hybridization and increased binding energy at the surface universally result in an enhancement of the 2 eV peak and a reduction of the E_F peak relative to the spin–orbit sideband. It has been demonstrated that quantitative separation of surface and bulk contributions to the *f*-spectral weight in angle-integrated valence band photoemission can be achieved by exploiting the variable electron escape depths at multiple photon energies [56], and that this surface and bulk decomposition is essential for an understanding of the spectra in relation to bulk thermodynamic properties [55]. Recent advances in energy resolution of valence photoemission at high photon energies (~1 keV) [20] where bulk sensitivity is enhanced, show promise for refinement of quantitative modeling of angle-integrated *f*-spectral weight.

In the course of this ARPES work at the 4*d* and 5*d* edges (~100 eV), we have accumulated various observations bearing on surface effects aided by the **k**-dependence of the spectra from different cleaves. To illustrate, Fig. 19 shows intensity images of on-resonance valence band spectra along Z–X–''Z'' for two different ''good'' and ''bad'' cleaved surfaces of $CeRu_2Si_2$. The ''good'' data in panel (a), an intensity representation of the same data as shown in Fig. 17(b), exhibit strongly dispersing *d*-band states

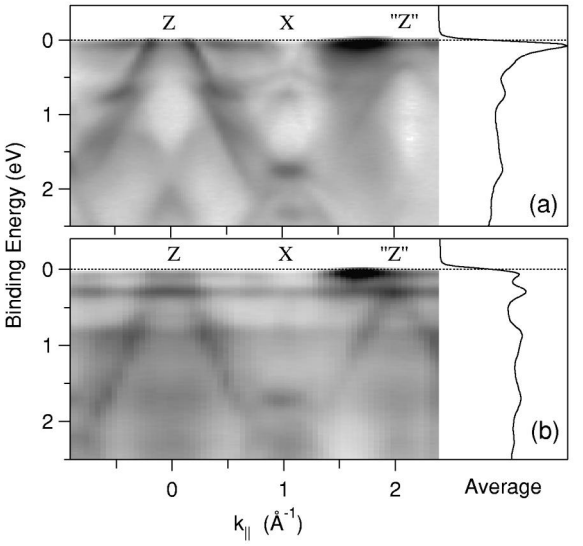

Fig. 19. Comparison of on-resonance valence spectra for $CeRu_2Si_2$ for two different cleave surfaces. The image in (a) is an intensity representation of the data in Fig. 17(b). Angle-averaged spectra for each data set are also shown.

and large *f*-weight intensity variation near E_F. The ''bad'' data in panel (b), in contrast, show streaks of **k**-independent spectral weight at 0.3, 0.8 and 1.6 eV binding energy, and a relatively smaller amplitude of dispersing *d*-bands and near-E_F *f*-states. The 0.3 eV peak corresponds to the Kondo sideband energy while the precise origin of the other two peaks is currently unknown. Also, since the reverse grayscale of each image has been separately adjusted to optimally enhance the intensity contrast, the $k_\parallel$-averaged spectrum of each data set has additionally been plotted in Fig. 19 for a more direct comparison of the different amplitude variations of the two cleaves. Also measured are multiple Si 2*p* core-level surface-shifted peaks with varying intensities from cleave to cleave. Such variations in Si 2*p* spectra and ARPES quality as illustrated in Fig. 19 occur not only between different cleaves, but also for different points on the same cleaved surface, probed using a 100 μm synchrotron beam spot, and with sample ''aging'' and/or poor vacuum.

We cannot make a unified picture yet, but there are two main considerations of: (i) different possible cleavage planes of $XRu_2Si_2(001)$ which contains an alternating atomic layering of –X–Si–Ru–Si–X–, and (ii) the different number of steps and edges contributing **k**-independent surface spectral weight. While the surface structure of the XRu_2Si_2 systems has not been experimentally determined yet, all cleaved surfaces exhibit sharp 1×1 LEED patterns indicating a lack of multi-zone reconstruction. Macroscopically rough regions on the cleaved surface will contain a significant enhancement of the surface area in general, especially of the edge-type of Ce atoms which lack long range order and which have smaller near-neighbor coordination leading to the spectral changes consistent with what is observed in Fig. 19(b). The correlation of Si 2*p* surface core-level shifts to valence spectra and to surface topography is a promising approach to further understanding of the surface structure.

Another important objective, which also involves the surface contribution, is to make connection back to angle-integrated resonant photoemission, a rather difficult task for single-crystal surfaces requiring the summing of spectra from many different angles. The averaged spectra in Fig. 19 show an initial step in this effort. It is very interesting to note that the ratio of the Kondo sideband to the main Kondo peak in the averaged spectrum in Fig. 19(a) is similar to that reported in a bulk-sensitive angle-integrated resonant photoemission study [20] at the Ce 3*d* edge, and the spectrum reported in Ref. [20] as being typical of resonant photoemission at the Ce 4*d* edge is similar to that of the poorer surface in Fig. 19(b). Thus, it may be that for $CeRu_2Si_2$ at least, spectra mostly characteristic of the bulk *can* be obtained at lower photon energy if the surface is sufficiently free of steps, edges, etc., or if the analysis area is very small. More complete angle-averaging efforts, comparison between Ce 3d and 4d edges, and correlation to Si 2*p* core-level shifts will be presented elsewhere.

5. Summary

The general picture that emerges from the experimental band structure measurements and FS maps of the XRu_2Si_2 intermetallic compounds with comparison to LDA calculations, is similar to that speculated in the discussion in Section 1.1. Namely, (i) good agreement with the *d*-band structure away from E_F is found for all compounds, (ii) relatively good agreement in the *d*-band derived FS contours is found for the f^0 compounds, especially for La, (iii) for X=Ce measured above its Kondo temperature, the FS appears to be essentially like that for La, and (iv) the near-E_F region for URu_2Si_2 is substantially different from theory. The equivalence of $LaRu_2Si_2$ and $CeRu_2Si_2$ Fermi surfaces suggests the exclusion of *f*-electrons from the FS in the high temperature state. The anomalous FS features in URu_2Si_2 can be traced to theoretical bands in the $ThRu_2Si_2$ electronic structure and suggest unrealistic disruptions of the *d*-band Fermi surface in LDA of f^2 systems.

Resonant ARPES of the Ce and U systems show extremely large variations in 4*f* and 5*f* spectral weights throughout the BZ. The FS mapping technique provides the global **k**-space view of the *f*-spectral weight that gives the relation to the underlying *d*-band structure and Fermi surface. Results include spectral signatures of Anderson lattice physics, e.g. the **k**-space confinement of *f*-spectral weight at the Fermi level to the interior of *d*-band hole Fermi surfaces signifies mixing of *d* and renormalized *f*-states. Detailed comparison of on-resonance spectra at isolated *d*-band crossings in $CeRu_2Si_2$ and URu_2Si_2 reveal differences in the *f*–*d*

spectral weight mixing qualitatively consistent with differences in the bulk heavy fermion properties. Visual hints of effective mass enhancement at E_F show promise for quantitative analysis. Finally, temperature-dependent resonant ARPES of URu_2Si_2 at a select region of **k**-space reveals a dramatic Kondo-like enhancement of the 5*f*-weight.

The many fundamental issues raised in the process of interpreting the current data of XRu_2Si_2 suggest that much more ARPES work is still to be done.

Acknowledgements

Work at U-M was supported by the U.S. DOE under Contract No. DE-FG02-90ER45416 and by the U.S. NSF Grant No. DMR-99-71611. Work at the Ames Lab was supported by the DOE under Contract No. W-7405-ENG-82. Work at UCSD was supported by NSF Grant No. DMR-97-05454. Work at the LANL was supported by the DOE. The SRC is supported by the U.S. NSF Grant No. DMR-95-31009, and the ALS by the U.S. DOE under Contract No. DE-AC03-76SF00098.

References

[1] P.A. Lee et al., Comments Conden. Matter Phys. 12 (1986) 99.
[2] W.R. Johanson, G.W. Crabtree, A.S. Edelstein, O.D. McMasters, Phys. Rev. Lett. 46 (1981) 504.
[3] R.M. Martin, J.W. Allen, Valence Fluctuations in Solids, North-Holland, Santa Barbara, 1981, p. 85.
[4] R.M. Martin, Phys. Rev. Lett. 48 (1982) 362.
[5] G. Zwicknagl, Adv. Phys. 41 (1992) 203.
[6] R. Eder, O. Rogojanu, G.A. Sawatzky, Phys. Rev. B 58 (1998) 7599.
[7] P.S. Riseborough, Phys. Rev. B 58 (1998) 15534.
[8] A.N. Tahvildar-Zadeh, M. Jarrell, J.K. Freericks, Phys. Rev. Lett. 80 (1998) 5168.
[9] J.W. Allen et al., Adv. Phys. 35 (1986) 275.
[10] D. Malterre, M. Grioni, Y. Baer, Adv. Phys. 45 (1996) 299.
[11] G.G. Lonzarich, J. Magn. Magn. Mater. 76–77 (1988) 1.
[12] Y. Onuki, in: T. Kasuya et al. (Ed.), Physical Properties of Actinide and Rare Earth Compounds, Jpn. J. Appl. Phys., 1993, p. 149.
[13] H. Kumigashira et al., Phys. Rev. B 54 (1996) 9341.
[14] T. Ito et al., Phys. Rev. B 60 (1999) 13390.
[15] A.B. Andrews et al., Phys. Rev. B 51 (1995) 3277.
[16] M. Garnier et al., Phys. Rev. B 56 (1997) R11399.
[17] A.J. Arko et al., Phys. Rev. B 56 (1997) R7041.
[18] A.J. Arko et al., in K.A. Gschneider Jr., L. Eyring (Eds.), Handbook on the Physics and Chemistry of Rare Earths, Vol. 26, Elsevier, Amsterdam, 1999, p. 265.
[19] M. Garnier et al., Phys. Rev. Lett. 78 (1997) 4127.
[20] A. Sekiyama et al., Nature 403 (2000) 396.
[21] J.D. Denlinger et al., Physica B 281–282 (2000) 716.
[22] G. Zwicknagl, Physica Scripta T49 (1993) 34.
[23] F.S. Tautz, S.R. Julian, G.J. McMullan, G.G. Lonzarich, Physica B 206–207 (1995) 29.
[24] T.T.M. Palstra et al., Phys. Rev. Lett. 55 (1985) 2727.
[25] M.B. Maple et al., Phys. Rev. Lett. 56 (1986) 185.
[26] H. Amitsuka et al., Physica B 281–282 (2000) 326.
[27] H. Yamagami, J. Phys. Soc. Jpn. 67 (1998) 3176.
[28] H. Yamagami, A. Hasegawa, J. Phys. Soc. Jpn. 59 (1990) 2426.
[29] H. Yamagami, A. Hasegawa, J. Phys. Soc. Jpn. 61 (1992) 2388.
[30] H. Yamagami, A. Hasegawa, J. Phys. Soc. Jpn. 62 (1993) 592.
[31] E.K.R. Runge, R.C. Albers, N.E. Christensen, G.E. Zwicknagl, Phys. Rev. B 51 (1995) 10375.
[32] G.J. Rozing, P.E. Mijnarends, D.D. Koelling, Phys. Rev. B 43 (1991) 9515.
[33] V.I. Anisimov, J. Zaanen, O.K. Andersen, Phys. Rev. B 44 (1991) 943.
[34] V.I. Anisimov, F. Aryasetiawan, A.I. Lichtenstein, J. Phys., Condens. Matter 9 (1997) 767.
[35] O. Gunnarsson, K. Schonhammer, in: K.A. Gschnieder Jr., L. Eyring, S. Hufner (Eds.), Handbook on the Physics and Chemistry of Rare Earths, Vol. 10, Elsevier, Amsterdam, 1987, p. 103.
[36] L. Taillefer, G.G. Lonzarich, Phys. Rev. Lett. 60 (1988) 1570.
[37] M.R. Norman, R.C. Albers, A.M. Boring, N.E. Christensen, Solid State Commun. 68 (1988) 245.
[38] H. Ohkuni et al., Phil. Mag. B 79 (1999) 1045.
[39] H. Yamagami, N. Hamada, Physica B 284–288 (2000) 1295.
[40] H. Aoki, S. Uji, A.K. Albessard, Y. Onuki, Phys. Rev. Lett. 71 (1993) 2110.
[41] C.A. King, G.G. Lonzarich, Physica B 171 (1991) 161.
[42] F.J. Himpsel, Adv. Phys. 32 (1983) 1.
[43] W. Bardyszewski, L. Hedin, Phys. Scr. 32 (1985) 439.
[44] F.J. Himpsel et al., Phys. Rev. Lett. 68 (1992) 3611.
[45] P. Aebi et al., Phys. Rev. Lett. 72 (1994) 2757.
[46] H. Nishimoto et al., J. Phys., Condens. Matter 8 (1996) 2715.
[47] J. Osterwalder, Surf. Rev. Lett. 4 (1997) 391.
[48] O. Gunnarsson et al., this volume.
[49] L.H. Tjeng et al., Phys. Rev. Lett. 71 (1993) 1419.
[50] D.P. Moore et al., Phys. Rev. B 62 (2000) 16492.
[51] D.A. Bonn, J.D. Garrett, T. Timusk, Phys. Rev. Lett. 61 (1988) 1305.
[52] J.G. Rodrigo, F. Guinea, S. Vieira, F.G. Aliev, Phys. Rev. B 55 (1997) 14318.
[53] S.H. Yang et al., J. Electron Spectrosc. Relat. Phenom. 78 (1996) 143.
[54] C. Laubschat et al., Phys. Rev. Lett. 65 (1990) 1639.
[55] L.Z. Liu et al., Phys. Rev. B 45 (1992) 8934.
[56] L. Duo, Surf. Sci. Rep. 32 (1998) 233.